Three-Dimensional Calibration of Micromanipulators Using Stereo Vision

Yi Xiong(✉), Juha Hirvonen, and Pasi Kallio

Micro-and Nanosystems Research Group,
Department of Automation Science and Engineering,
Tampere University of Technology,
Korkeakoulunkatu 3,
33720 Tampere, Finland
Email: yi.xiong@ieee.org

Abstract— Calibration is of great significance in the development of automatic micromanipulation systems. This paper presents a novel vision based procedure for three-dimensional (3D) calibration of micromanipulators. Two major issues in the proposed calibration approach - vision system calibration and manipulator kinematic calibration - are discussed in detail in this paper. Verification and evaluation experiments are conducted using a 3D micromanipulator in a microrobotic fiber characterization platform. Experimental results demonstrate that the proposed calibration approach is able to achieve prediction errors below 5 μm. The proposed approach also demonstrates the feasibility of calibrating the decoupled motions, by reducing the undesired movement from 28 μm to 8 μm (for 4800 μm desired movement).

Keywords- Micromanipulator Calibration; Computer Vision; Automation; Micromanipulation; Kinematics

1 Introduction

Within the last decade, the development of automatic microrobotic systems has become an active area of research, and has evolved into a significant sector in microengineering. Microrobotics is a multidisciplinary field that develops miniaturized robotic systems with either overall size or precision at a microscopic level. Currently, the research focuses on two main areas: microrobotic agents; and micromanipulation and microhandling. Micromanipulation and microhandling concern handling of micro-objects that range from one micrometer to few millimeters. The main applications include:

- living cell manipulation in bioengineering [1–2],
- micro-electro-mechanical systems(MEMS)/micro-opto-electro-mechanical systems (MOEMS) assembly in semiconductor manufacturing [3–4] and
- micro- and nanoscale material characterization in material sciences [5–6].

Conventionally, those tasks are manually conducted by skilled operators. However, the process is tedious, time-consuming and with a low success rate. Thus, high-yield automatic micromanipulation systems have been extensively studied and well-funded in the past decade [7–9]. Nowadays, the research on micromanipulation and microhandling has shifted its scope from the conceptual system development to industrial applications. Consequently, the future development of this field lies in the industrial applicability of systems that aim to convert the micromanipulation technique to a high throughput process.

Since the tolerance bands are narrow in the microscale (typically less than 10 µm for positioning and hundreds of µN for force), position and force control are considered two major challenges in developing micromanipulation systems. The motivation for this paper stems from the investigation on improving the positioning accuracy of a micromanipulation system. The positioning accuracy directly affects whether the devices or target objects can be positioned into the narrow tolerance band, and so decides the success or failure of a micromanipulation operation. Actions can be taken from either the hardware or software aspect to improve the positioning accuracy.

One hardware solution is to increase the precision of a micro actuator by novel actuation principles and mechanisms. Furthermore, it is also possible to improve the positioning accuracy of the micromanipulator by controlling the ambient variables, including humidity, temperature, and vibrations. In [10],

characterization, modeling and reducing environmental noise in a micromanipulation system have been studied. In another study [11], a microassembly station with a controlled environment and vibration isolation demonstrates a better performance. Nevertheless, manufacturing imperfections, alignment errors, and component wearing will inevitably introduce positioning errors. In addition, the cost is much higher to compensate for such errors by a hardware-based approach rather than using a software-based approach.

According to the opinions in [12], calibration and visual servoing are two main streams in the software-based approach. Elegant methods have been developed to calibrate the position and orientation of a micromanipulator [13–15]. Meanwhile, several other two-dimensional (2D) calibration approaches [16–18] have been proposed for a vision guided micromanipulation system in the application areas of cell microinjection and microassembly. Moreover, a three-dimensional (3D) calibration method utilizing a laser sensor is described in [19]. However, such a calibration method, which needs to rotate the entire platform, is not as suitable in practical operations, since the platform needs to be calibrated whenever the configurations are changed. Table 1 lists the most representative studies in the field of microrobotic calibration.

This paper proposes a vision-based 3D calibration method for a micromanipulation platform which is experimentally verified using a micromanipulation system developed in Micro- and Nano System Research Group (MST) at Tampere University of Technology (TUT) [5] [21–22]. The paper is structured as follows. Section 2 provides a brief introduction of the micromanipulation system and schematically introduces the coordinate frames. Section 3 and Section 4 present a generic scheme for vision-based microrobotics calibration and a detailed description for both camera calibration and manipulator kinematics calibration. Section 5 demonstrates the experimental results by applying the calibration method on the microrobotic fiber characterization platform. Section 6 discusses the novelties and limitations of the proposed approach. Finally, Section 7 discusses results and conclusions.

2 Micromanipulation Platform

The micromanipulation platform used in this work is developed as a novel tool for wood derived fiber characterization. The objective is to automatically manipulate

and characterize individual fibers and fiber bonds in a high throughput. The teleoperated fiber characterization process has been successfully demonstrated on this platform. The next phase of the system development aims to transfer the system from teleoperated control toward autonomous control. The system has a Stacked Gantry Crane configuration and includes two SmarAct microgrippers, an XY-table with a rotary table (SmarAct SR-1908) and a micro-force sensor (FemtoTools FT-S54). All the tailored micromanipulators are composed of several individual linear actuators. Furthermore, all the linear actuators mentioned above are piezoelectric stick-slip type microactuators provided with a local feedback control system purchased from SmarAct GmbH. In addition, the system uses two cameras (Sony XCD-U100 and AVT Manta G-504B) with optics to monitor the operation area using top and side views. In the fiber characterization process, the fibers are initially placed in a fiber bank located on the top of the rotary table. The micromanipulators are used for picking up a fiber from both ends and then for synchronously moving it to the microsensor for characterization. Fig. 1 provides an overview of the platform.

Since the calibration procedure involves several coordinate frames in the micromanipulation system, they are schematically introduced first. This paper focuses on deriving the direct and inverse kinematics of Micromanipulator 1 (No. 3 in Fig. 1) used for positioning Microgripper (No. 5 in Fig. 1).

As shown in Fig. 2, the definitions and notations of the relevant coordinate systems are:

- End-effector frame $\{E\}$: The origin of the frame is located at a virtual point which is described in Section 4. The x and y axes are respectively aligned with the rows and columns of a chessboard, which is attached to the micromanipulator.$\{E\text{-}(1)\}$ and $E\text{-}(2)\}$ refer to the locations of end-effector frame at the initial position and a desired position, respectively.
- Base frame $\{B\}$: The frame is identical to the initial pose of the end-effector frame $\{E\text{-}(1)\}$ when all the joint variables are zero.
- Image frames $\{I1\}$, $\{I2\}$: The image frames describe a 2D coordinate system. They are identical to the local coordinate systems on the CCD image arrays of the top and side view cameras, respectively.
- Vision system frame $\{V\}$: The origin of this frame is affixed to a feature point in a dot grid which is used in the vision system calibration described

in Section 3. The x axis is aligned with the rows of the dot grid and the y axis with the columns of the dot grid.

- Object frame $\{O\}$: The object frame is located on a desired point of object.

For control purposes, it is convenient to describe all the points and vectors in the same reference frame. Here, the vision system frame is selected as the reference frame. The calibration of microrobotics system aims to compute the relationship between the vision system frame and the other frames. Determining the geometric transformation from the 2D image frames $\{I1\}$, $\{I2\}$ to the 3D vision system frame $\{V\}$ is termed vision system calibration. Additionally, the positions of the end-effector frame $\{E\}$ and the base frame $\{B\}$ are both known in regard to the image frames $\{I1\}$, $\{I2\}$. Therefore, the relation between those frames and the 3D vision system frame $\{V\}$ can be determined. On the other hand, estimating the geometric transformation from the end-effector frame $\{E\}$ to the base frame $\{B\}$ is called manipulator kinematic calibration. Hence, the microrobotics system calibration comprises two major issues: vision system calibration and manipulator kinematic calibration to be discussed in the following sections.

3 Vision System Calibration

The vision system in the micromanipulation platform monitors the micro-scale objects through the top and side views, which both use a microscope-camera system configuration to increase magnification. For each camera, the points in the 3D scene space are projected to the corresponding points on the 2D image planes. The depth information is lost during this process. Thus, the main task in the vision system calibration is to reconstruct the 3D information of the interest points from the 2D images. The first step of 3D vision reconstruction is calibrating the cameras and then recovering the depth information by triangulation.

3.1. Camera calibration

For calibrating a single camera, a significant number of robust and efficient methods can be found in the literature. Tsai [23] and Zhang [24] have proposed the two most classical approaches. In both cases, after the distortion compensation, the camera projection from a 3D point (X, Y, Z) point to a 2D point (x, y) is represented by a parametric model:

$$\begin{pmatrix} x \\ y \\ 1 \end{pmatrix} = \begin{bmatrix} f_x & 0 & c_x \\ 0 & f_y & c_y \\ 0 & 0 & 1 \end{bmatrix} \begin{bmatrix} 1 & 0 & 0 & 0 \\ 0 & 1 & 0 & 0 \\ 0 & 0 & 1 & 0 \end{bmatrix} \begin{bmatrix} \mathbf{R} & \mathbf{T} \\ \mathbf{0}_{3\mathrm{x}1} & 1 \end{bmatrix} \begin{pmatrix} X \\ Y \\ Z \\ 1 \end{pmatrix}, \tag{1}$$

where, the parameters can be divided into two groups:

Extrinsic parameters:

1) **R** is a 3×3 rotation matrix;
2) **T** is a 3×1 translation matrix.

Intrinsic parameters:

1) f_x is the focal length in horizontal direction;
2) f_y is the focal length in vertical direction;
3) (c_x , c_y) is the location of a principle point, where the optic axis intersects the image plane.

In this work, a group of images on a dot grid is taken at different poses and used for recovering the intrinsic and extrinsic coefficients in the parametric model. We denote a 3×4 camera matrix **P** as:

$$\mathbf{P} = \mathbf{K}\langle \mathbf{R} | \mathbf{T} \rangle = \mathbf{K}\mathbf{R}\langle \mathbf{I} | \mathbf{R}^{\mathrm{T}}\mathbf{T} \rangle, \tag{2}$$

where,

$$\mathbf{K} = \begin{bmatrix} f_x & 0 & c_x \\ 0 & f_y & c_y \\ 0 & 0 & 1 \end{bmatrix}. \tag{3}$$

Consequently, the 3D to 2D camera projection has a concise form:

$$\mathbf{x} = \mathbf{P}\mathbf{X}, \tag{4}$$

where **X** and **x** are the coordinate vectors of a 3D point and a corresponding image point, respectively.

3.2. Three dimensional reconstruction

As shown in Fig. 3, in essence, the stereo imaging system comprises two cameras at different locations. The points x and x' are both 2D images of the point X in 3D space.

With the previous knowledge, each camera can be described by the 3×4 camera matrices **P** and $\mathbf{P}'$ respectively:

$$\begin{aligned} \mathbf{x} &= \mathbf{P}\mathbf{X} \\ \mathbf{x}' &= \mathbf{P}'\mathbf{X} \end{aligned} \tag{5}$$

Typically, the next step in the 3D reconstruction is to compute point correspondences based on the epipolar geometry. However, it is unnecessary to find out the point correspondences in this case, as the dot grid is used here.

If the *n*-th row of the matrix **P** ($\mathbf{P}'$) is denoted by p^{NT} (p'^{NT}), Equation (5) can be rewritten as linear equations in **X**:

$$\mathbf{AX} = \begin{bmatrix} xp^{3T} - p^{1T} \\ yp^{3T} - p^{2T} \\ x'p'^{3T} - p'^{1T} \\ y'p'^{3T} - p'^{2T} \end{bmatrix} \mathbf{X} = 0 \tag{6}$$

This equation can be solved using the direct linear transformation (DLT) algorithm to obtain a least-square solution. Therefore, the algorithm for reconstructing the 3D coordinates in the vision frame can be described as:

1) Form equation **AX**=0
2) Decompose the matrix **A** into three sub matrices **U**, **D, V**$^{\mathbf{T}}$ using the singular value decomposition .
3) **A** has the dimension 4×3 and rank 3, and it has a one-dimensional null space that provides a solution for **X**.

Consequently, the homogenous coordinates of the 3D point after reconstruction is derived as the smallest singular value of matrix **A**, which is the last column of **V**.

4 Manipulator Kinematic Calibration

This section concentrates on the manipulator kinematic calibration, based on the 3D calibration of the vision system. In general, the kinematic calibration consists of four steps: direct kinematic modeling, data acquisition, parameter estimation and compensation (inverse kinematics) implementation.

4.1. Kinematic modeling

Several well-honed approaches to develop a direct kinematic model for serial manipulators have been proposed, including the Denavit-Hartenberg (D-H) method. According to the model structures, methods can be roughly divided into white-box modeling and black-box modeling. The first approach is based on geometric relationship. The second is an empirical model that is estimated based on input and output information. This approach is an implicit method which "masks" the geometric relationship into coefficients of the model. However, since

the joint geometric dimensions are difficult or even impossible to be accurately measured in micro scale, the geometry based modeling is not sufficient in our case. Therefore, the black-box approach is employed for the direct kinematic modeling.

In many previous studies, the transformation model between the end-effector frame and the base frame is typically described as a linear function of individual joint variables. However, in practice, some geometric or non-geometric factors such as straightness error and periodical disturbances may not only follow a first-order function but also a high order function of the joint variables. Thus, the second-order terms of the joint variables have been introduced in the model as follows:

$$\begin{bmatrix} {}^{V}X_E \\ {}^{V}Y_E \\ {}^{V}Z_E \end{bmatrix} = \begin{bmatrix} a_1 & a_2 & a_3 \\ b_1 & b_2 & b_3 \\ c_1 & c_2 & c_3 \end{bmatrix} \begin{bmatrix} d_x \\ d_y \\ d_z \end{bmatrix} + \begin{bmatrix} a_4 & a_5 & a_6 \\ b_4 & b_5 & b_6 \\ c_4 & c_5 & c_6 \end{bmatrix} \begin{bmatrix} d_x^{\,2} \\ d_y^{\,2} \\ d_z^{\,2} \end{bmatrix} + \begin{bmatrix} a_7 & a_8 & a_9 \\ b_7 & b_8 & b_9 \\ c_7 & c_8 & c_9 \end{bmatrix} \begin{bmatrix} d_x \cdot d_y \\ d_y \cdot d_z \\ d_x \cdot d_z \end{bmatrix} + \begin{bmatrix} a_{10} \\ b_{10} \\ c_{10} \end{bmatrix} + \begin{bmatrix} {}^{V}X_B \\ {}^{V}Y_B \\ {}^{V}Z_B \end{bmatrix}, \quad (7)$$

where, $[{}^{V}X_E,\ {}^{V}Y_E,\ {}^{V}Z_E]^T$ and $[{}^{V}X_B,\ {}^{V}Y_B,\ {}^{V}Z_B]^T$ are the locations of the end-effector frame $\{E\}$ and the base frame$\{B\}$ in the vision frame $\{V\}$, respectively. Vector $\mathbf{\Theta} = [d_x,\ d_y,\ d_z]^T$ represents the joint variables of the individual actuators along the x, y and z axes. In addition, 30 unknown parameters are defined with three vectors: $\mathbf{A} = [a_1,\ a_2 \ldots a_{10}]$, $\mathbf{B} = [b_1,\ b_2 \ldots b_{10}]$, and $\mathbf{C} = [c_1,\ c_2 \ldots c_{10}]$.

By expanding Equation (7), the coordinates of the end-effector can be determined in the vision frame as follows:

$${}^{V}X_E = a_1 d_x + a_2 d_y + a_3 d_z + a_4 d_x^{\,2} + a_5 d_y^{\,2} + a_6 d_z^{\,2} + a_7 d_x d_y + a_8 d_y d_z + a_9 d_x d_z + a_{10} + {}^{V}X_B \quad (8)$$

$${}^{V}Y_E = b_1 d_x + b_2 d_y + b_3 d_z + b_4 d_x^{\,2} + b_5 d_y^{\,2} + b_6 d_z^{\,2} + b_7 d_x d_y + b_8 d_y d_z + b_9 d_x d_z + b_{10} + {}^{V}Y_B \quad (9)$$

$${}^{V}Z_E = c_1 d_x + c_2 d_y + c_3 d_z + c_4 d_x^{\,2} + c_5 d_y^{\,2} + c_6 d_z^{\,2} + c_7 d_x d_y + c_8 d_y d_z + c_9 d_x d_z + c_{10} + {}^{V}Z_B \quad (10)$$

The polynomial model has several advantages, compared with other models. First of all, this model can be extended by adding extra terms if additional factors show significant impacts on the end-effector location. On the other hand, the model can be simplified by eliminating non-effective terms by applying stepwise regression which will be described in Section 4.3.

4.2. Data acquisition

In this step, the correspondences including the joint inputs and the positions of the end-effector in the vision frame are collected. Compared with the joint inputs, which can be easily recorded in the actuators, the positions of the end-effector are more challenging to determine. Many efforts have been made to improve the accuracy and reliability of the end-effector position measurement. In [13], the problem was solved using a local illumination system by lighting the end-effector with an optical fiber. In a similar way, [25] used two infrared LEDs mounted on the bottom of a robot to measure the end-effector positions. Since a gripper jaw acts as the end-effector in our platform, it is difficult to identify the same reference point on the jaw every time. Motivated by the vision system calibration, a chessboard pattern is attached to the gripper for indirectly measuring the end-effector position in the global frame [21]. As shown in Fig. 4, the spatial relationship between the chessboard frame $\{C\}$ and the jaw frame $\{J\}$ is stationary. Hence, the end-effector frame $\{E\}$ is located on the chessboard rather than on the gripper jaw.

This approach has the following advantages:

- The chessboard pattern, which includes high contrast line and corner features, is easily detected.
- It is straightforward and convenient to set the correspondence between the corner features on the physical chessboard and the image.
- Ready-to-use functions that are able to measure features from images with sub-pixel accuracy are available in third-party libraries (e.g. OpenCV [26] and Camera Calibration Toolbox for Matlab)

In the beginning, only one extracted corner that represents the end-effector is used to calculate the position in the workspace. Ideally, if the movement of the chessboard keeps constant, the spatial distances between corners in the two images should have the same value. However, as shown in Table 2, the standard derivations of the measurements are 0.207 pixels and 0.172 pixels on x and y directions, respectively. The results imply that the repeatability of the measurement needs to be improved. Thus, a virtual point $[P_v^x, P_v^y]$ calculated from the locations of all the chessboard inner corners represents the end-effector:

$$P_v^X = \frac{\sum_{i=1}^{N} P_i^X}{N} \quad P_v^Y = \frac{\sum_{i=1}^{N} P_i^Y}{N}, \tag{11}$$

where, [P_i^x , P_i^y] is the location of the inner corner *i* in the 2D image frame. Since small measurement errors cancel out each other by taking the mean value of several feature points, standard deviations are reduced to 0.087 pixels and 0.045 pixels on *x* and *y* directions, respectively.

A trajectory command that consists of 170 random movements in the direction of all the axes is automatically generated by the computer. The generated command must have as many different robot configurations as possible to gain a proper kinematic model (Fig. 5).

4.3. Parameter estimation

As observed in the candidate model, the relationship between the actuator inputs and the end-effector positions is a second-order nonlinear function. Furthermore, since the model is not based on physical modeling, the significance of each input term (actuator inputs) to the output (end-effector positions) is unknown. Thus, an algorithm is needed that can not only estimate coefficient values but also eliminate the least significant terms.

Stepwise algorithm as an automatic procedure for statistic model selection is able to meet the aforementioned requirements. The candidate variables will each be tested for their statistical significance with *F*-tests to decide if the variables are to be included or excluded [27]. Therefore, the stepwise algorithm is especially suitable, since the model has a large number of potential explanatory variables. The method proceeds as follows:

1) Calculate the correlation of all the variables with the output. Select the one with the highest correlation as the first variable to enter the test. The variable is retained if it can pass the overall F-test.
2) Calculate the partial correlation of the remaining variables. Choose the one with highest partial correlation to enter the test. Similar to Step 1, the term is retained if it can pass the overall F-test.
3) Repeat Step 2 until all potential variables have been tested. All parameters are iteratively refined based on their statistical significance.

This algorithm is provided as a ready-to-use function in Statistic Toolbox in Matlab.

4.4. Compensation implementation

Since the polynomial model consists of second-order terms, it is obvious that the inverse kinematic equations cannot be implicitly expressed as a function of the desired end-effector position $[{}^{V}X_E, {}^{V}Y_E, {}^{V}Z_E]^T$. A parameter optimization tool is needed to find a solution $\mathbf{\Theta}=[d_x, d_y, d_z]$, so that the nonlinear function:

$$F = f([{}^{V}X_B, {}^{V}Y_B, {}^{V}Z_B], \mathbf{\Theta}, \mathbf{A}, \mathbf{B}, \mathbf{C}) - [{}^{V}X_E, {}^{V}Y_E, {}^{V}Z_E] \quad (12)$$

can be converged. Since the number of unknowns is equal to the number of equations, the problem is categorized as an equality-constrained optimization problem.

Several well-studied algorithms are suitable to handle such problems, including the Gauss-Newton method, the Levenberg-Marquardt method (also called a trust-region method), QR decomposition and Singular value decomposition. In general, all those methods first approximate the nonlinear model to be linear, and refine the parameters after several iterations. The Gauss-Newton and Levenberg-Marquardt methods use the same principle by starting with an initial value and then moving to a certain direction within iterations to minimize the normal function. However, the difference between the two methods is that the Levenberg-Marquardt algorithm is able to handle divergence when the shift vector is far from the correct direction. QR decomposition and singular value decomposition methods belong to a matrix computation approach that does not involve forming the normal equations.

Since ready-to-use functions are available in the Optimization Toolbox of Matlab, the Levenberg-Marquardt method is selected in this paper. Heretofore, an optimal compensator as an inverse kinematic model is formulated as shown in Fig. 6. The optimal compensator is derived based on the direct kinematic model derived in the previous sections.

5 Experimental Results

An experiment is conducted on the micromanipulation platform to verify the feasibility and evaluate the performance of the proposed automatic calibration procedure

5.1. Results of vision system calibration

Following the calibration procedure in Section 3, the camera matrices for the top and side view cameras are computed as:

$$\mathbf{P} = \begin{bmatrix} 1.94e+04 & -5.47e+02 & 7.09e+02 & 1.61e+05 \\ 4.30e+01 & 1.17e+04 & 8.83e+03 & 7.93e+04 \\ -6.28e-03 & -5.67e-01 & 8.23e-01 & 3.24e+02 \end{bmatrix}$$

$$\mathbf{P}' = \begin{bmatrix} 1.28e+04 & 1.45e+02 & -4.54e+02 & 8.41e+04 \\ -9.99e+01 & 1.28e+04 & 5.45e+02 & 4.13e+04 \\ 8.51e-02 & -1.52e-04 & 9.96e-01 & 2.84e+02 \end{bmatrix}$$

5.2. Results of kinematic calibration

The trajectory command including 170 random movements with different configurations was used as an input for the micromanipulator. Corresponding locations of the end-effector in the vision frame were collected. In the measurement set, 110 points are used for the calibration and 60 points are used for the model validation.

After the calibration procedure, the coefficients of the polynomial model are estimated as:

$$\mathbf{A} = [1.000893 \quad 0 \quad 0.002475 \quad 0 \quad -4.74e-08 \quad 0 \quad 0 \quad 0 \quad 0]$$

$$\mathbf{B} = [0 \quad 0.999927 \quad 0 \quad 0 \quad 0 \quad 0 \quad 7.11e-07 \quad 0 \quad 0]$$

$$\mathbf{C} = [0.000874 \quad 0 \quad 1.000775 \quad 0 \quad 0 \quad 0 \quad 0 \quad 0 \quad 0]$$

It should be noted that some coefficients show a zero value. Such terms are eliminated in the polynomial kinematic model, since their static significances are low.

According to the ISO 9283 robot performance standard, the prediction error is expressed as the spatial distance between the predicted poses and the desired pose, and it can be computed as follows:

$$PE = \sqrt{(x_i - \hat{x}_i)^2 + (y_i - \hat{y}_i)^2 + (z_i - \hat{z}_i)^2} \tag{13}$$

where, (x_i, y_i, z_i) are the actual positions measured by the vision system, and $(\hat{x}_i, \hat{y}_i, \hat{z}_i)$ are the corresponding positions predicted with the kinematic model. The prediction error of 60 validation points are computed and illustrated in Fig. 7.

The experimental results demonstrate that the maximum model prediction error is smaller than 5 micrometers. The mean value and standard deviation of the position error are approximately 2.59 micrometers and 1.32 micrometers, respectively.

5.3. Decoupling test

Until now, the forward kinematic model has been calibrated and evaluated through the cross-validation test. The next step is implementing the micromanipulator compensation based on the control scheme depicted in Fig. 6.In order to further examine the ability of the calibrated micromanipulator to produce decoupled motions, decoupling tests are carried out with and without the calibration. The test is designed as follows: the micromanipulator is commanded to move 8000 micrometers along the *x* axis, 8000 micrometers along the *y* axis and 4800 micrometers along the *z* axis, as shown in Fig. 8.

In an ideal case, the motion in a single direction should not affect the other movement along the other two axes. In other words, the displacements of the micromanipulator in *y* and *z* directions should be zero when it moves along the *x* direction; and so on. However, the test results demonstrate that interactions exist among the motions of three axes (depicted in Fig. 9). As shown in Fig. 9-(a), the unwanted displacements in the *x* direction, caused by the motions in *y* and *z* directions, are a maximum of -6.144μm and -0.104μm, respectively. Fig. 9-(b) implies the unwanted displacements in the y direction, caused by the motion in *x* and *z* directions, as -25.13μm and -3.21μm. Fig. 9-(c) depicts that the maximum unwanted displacements in the z direction, caused by the motion in *x* and *y* directions, are -4.68μm and 10.55μm, respectively. The maximum unwanted displacement, approximately -25.13 μm, is in the y direction when the micromanipulator moves along the *z* direction for 4800μm.

The input signals to the actuators are pre-shaped with the optimal compensator, (Fig. 5) to reduce the interaction among the motions along the three axes.

Fig. 10 shows the measured displacements of the micromanipulator for the decoupled motions, when using the optimal compensator. When the micromanipulator moves along the *y* and *z* directions, the unwanted displacements in the *x* direction are reduced to -4.33μm and 0.21μm, respectively. The maximum unwanted displacements in the *y* direction during the movement in the

x and *z* directions are -5.11μm and 3.64μm, approximately 60% smaller than in the uncalibrated case. When the micromanipulator is driving along the *x* and *y* directions, the unwanted displacement is reduced to -0.71μm and 5.986μm, respectively

To summarize, the ability of the micromanipulator to produce decoupled motions is improved using the inverse kinematics calibration of the micromanipulator. The results show that undesired displacements for the decoupled motions are all reduced. However, the percentages of the improvement vary along the three axes. Maximum reduction is approximately 60% in the *y* direction and minimum reduction is approximately 13% in the *z* direction. The results show that the designed calibrator is able to reduce the kinematic errors of the micromanipulator, but the performance improvement is naturally limited if the kinematic error is smaller than the measurement error. However, the result in the *y* direction demonstrates that an error larger than 10 μm can be significantly reduced with the proposed calibration approach.

6 Discussions

The experimental results presented in this paper validate the proposed calibration approach and demonstrate the ability to reduce static errors to an acceptable level. Compared with other documented methods, the proposed procedure has several novelties.

1. It is the first to introduce a stereo vision measurement system for 3D microrobot calibration. In previous studies, depth information has been estimated through auto-focusing techniques. However, since a stack of images needed to be acquired and processed, the whole process took a considerable time. Moreover, the measurement result was not sufficiently accurate and robust. Lacking those disadvantages, the stereo vision measurement system is also easy to use and fast to implement.

2. In the approach proposed here, a chessboard pattern is not only used as a calibration board for the camera calibration but also as a target object for the microrobot calibration. More detailed discussions of the advantages are included in Section 3.

There are several points to consider in future studies.

The limitation of the vision system: The results, currently theoretically limited by the resolution of the optical systems in use, can be further improved using high precision instruments. According to the Rayleigh criterion, the resolution of optical systems with the light microscope can be down to 200 nm. However, it can be anticipated that the field of view will be limited, so a microfabricated calibration pattern with a more compact size and a higher accuracy is needed to calibrate the vision system.

The limitation of the control scheme: In the vision-based feedforward control scheme, static system errors, such as manufacturing imperfections, alignment errors, and component wearing can be overcome using the kinematic calibration. However, the unpredictable disturbances and dynamic errors cannot be efficiently eliminated without closed-loop control schemes such as visual servoing. However, computational time and real-time ability need to be taken into account with these schemes. Therefore, compromise should be made between the feedforward and closed-loop schemes.

7 Conclusions

In this paper, a novel vision based automatic calibration approach is proposed for a serial-type micromanipulator. The whole calibration procedure is carried out using two steps: vision system calibration and manipulator kinematic calibration. First, the vision system calibration is carried out using single camera calibration and 3D image reconstruction. Then, the kinematic calibration of the micromanipulator is performed in four steps: kinematic modeling, data acquisition, parameter estimation, and compensation implementation.

The proposed automatic calibration approach has been verified on a microrobotic fiber characterization platform. Evaluated by the cross validation set data, the prediction errors with 5 μm maximum have been achieved using the polynomial model. In a decoupling test, the maximum undesired displacement is observed in the *y* direction when the micromanipulator moves along the *z* direction. The undesired displacement is reduced from -25.13 μm to -5.11 μm using the proposed optimal compensator.

ACKNOWLEDGMENT

The authors would like to thank the Finnish Funding Agency for Technology and Innovation (Tekes) (grant number 40415/08) and The Academy of Finland (grant numbers 253364 and 256527) for their financial support.

REFERENCES

1. Wang W, Liu X, Gelinas BD, Sun Y (2007) A fully automated robotic system for microinjection of zebrafish embryos. In: PLoS ONE, Vol.2, No.9

2. Kallio P, Kuncova-Kallio J (2006) Capillary pressure microinjection of living adherent cells: challenges in automation. In: Journal of Micromechatronics, Vol. 3, pp. 189-220

3. Dechev N, Ren L, Liu W, Cleghorn WL, Mills JK (2006) Development of a 6 degree of freedom robotic micromanipulator for use in 3D MEMS microassembly. In: IEEE International Conference on Robotics and Automation, ICRA

4. Popa D, Murthy R, Mitta M, Sin J and Stephanou H (2006) M3-modular multi-scale assembly system for MEMS packaging. In: IEEE/RSJ International Conference on Intelligent Robots and Systems, IROS

5. Saketi P, Treimanis A, Fardim P, Ronkanen P, Kallio P (2010) Microrobotic platform for manipulation and flexibility measurement of individual paper fibers. In: IEEE/RSJ International Conference on Intelligent Robots and Systems, IROS

6. Stolle C, Bartenwerfer M, Celle C, Simonato JP, Fatikow S (2012) Nanorobotic strategies for handling and characterization of metal-assisted etched silicon nanowires. In: IEEE/ASME Transactions on Mechatronics

7. Gauthier M and Régnier S (2010) Robotic Micro-assembly, IEEE Press

8. Nelson BJ, Dong LX, Arai F (2008)Micro/Nanorobotics. In: Springer Handbook of Robotics, 1st Ed., Heidelberg, Springer-Verlag GmbH

9. Chaillet N, Régnier S (2010) Microrobotics for Micromanipulation, Wiley-ISTE

10. Haddab Y, Gorrec YL, Lutz P (2011) Effects of environmental noise on the accuracy of millimeter sized grippers in cantilever configuration and active stabilization. In: IEEE International Conference on Robotics and Automation, ICRA

11. Zhou Q, Aurelian A, Corral CD, Esteban PJ (2011) A microassembly station with controlled environment. In: Microrobotics and Microassembly, SPIE

12. Fukuda T, Arai F (1998) Micromanipulation and robotic technology. In: Technical Proceedings of the 1998 International Conference on Modeling and Simulation of Microsystems

13. Kawaji A, Arai F, Fukuda T (1999) Calibration for contact type of micro-manipulation. In: IEEE/RSJ International Conference on Intelligent Robots and Systems, IROS

14. Li G, Xi N (2002) Calibration of a micromanipulation system. In IEEE/RSJ International Conference on Intelligent Robots and Systems, IROS

15. Liu X, Lu Z, Sun Y (2011) Orientation control of biological cells under inverted microscopy. In: IEEE/ASME Transactions on Mechatronics

16. Zhang Y, Han M, Shee C, Chia T, Ang W (2009) Self-calibration method for vision-guided cell micromanipulation system. In: Journal of Microscopy (233):340-345

17. Mattos LS, Caldwell DG (2009) A fast and precise micropipette positioning system based on continuous camera-robot recalibration and visual servoing. In: 5th IEEE Conference on Automation Science and Engineering
18. Tan N, Clevy C, Laurent GJ, Chaillet N (2012) Calibration and validation of XYΘ micropositioners with vision. In: IEEE/ASME International Conference on Advanced Intelligent Mechatronics, AIM
19. Zhou Q, Korhonen P, Jukka L, Sjoval S (2006) Automatic dexterous microhandling based on a 6 DOF microgripper. In: Journal of Micromechatronics
20. Arai T, Larsonneur R, Jaya Y (1993) Calibration and basic motion of a micro hand module. In: International Conference on Industrial Electronics, Control, and Instrumentation
21. Essen M, Hirvonen J, Saketi P, Kallio P (2011) Automated grasping in manipulation of individual paper fibers. In: International Conference on Manipulation, Manufacturing and Measurement on the Nanoscale, 3M-Nano
22. Saketi P, Kallio P (2011) Microrobotic platform for making, manipulating and breaking individual paper fiber bonds. In: International Symposium on Assembly and Manufacturing
23. Tsai R (1987) A versatile camera calibration technique for high accuracy 3D machine vision metrology using off-the-shelf TV cameras and lens. In: IEEE Journal of Robotics and Automation,
24. Zhang Z (2000) Calibration, a flexible new technique for camera. In: IEEE Transactions on Pattern Analysis and Machine Intelligence
25. Fatikow S, Stolle C, Diederichs C, Jasper D (2011) Auto-configuration and self-calibration in flexible robot-based micro/nanohandling Cells. In: International Federation of Automatic Control
26. OpenCV v2.4.0-beta2 documentation (2012) Available:
http://opencv.itseez.com/trunk/index.html. [Accessed 27 04 2012].
27. Draper N, Smith H (1981), Applied Regression Analysis, 2 ed., New York: John Wiley & Sons, Inc

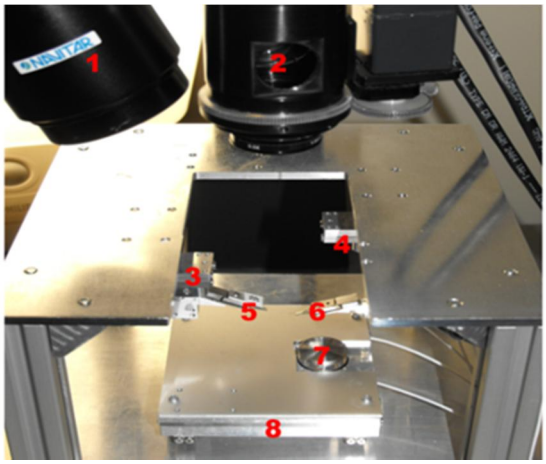

Fig. 1 The microrobotic platform used for fiber characterization: top view camera (1), side view camera (2), micromanipulators (3,4) microgrippers (5, 6), rotary table (7), and *X*-*Y* positioning table (8).

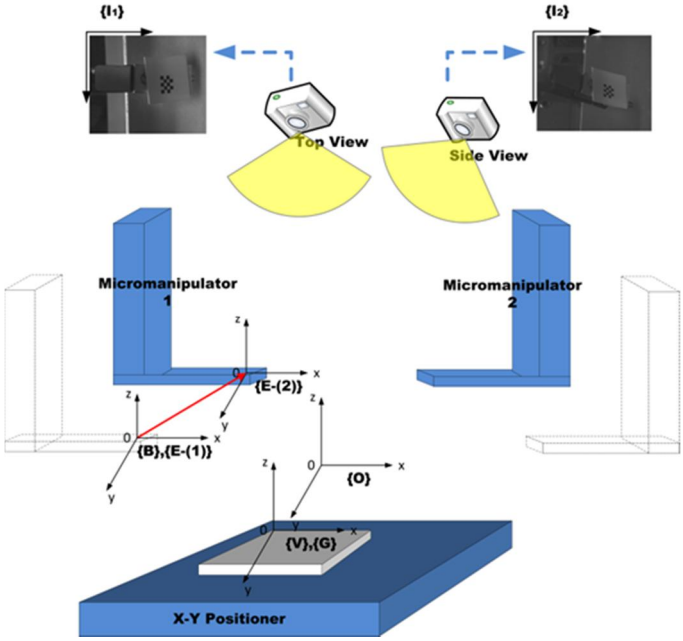

Fig. 2 Coordinate frame assignment in the microrobotic platform

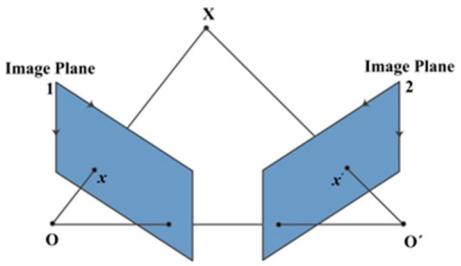

Fig. 3 The geometry of the stereo vision system

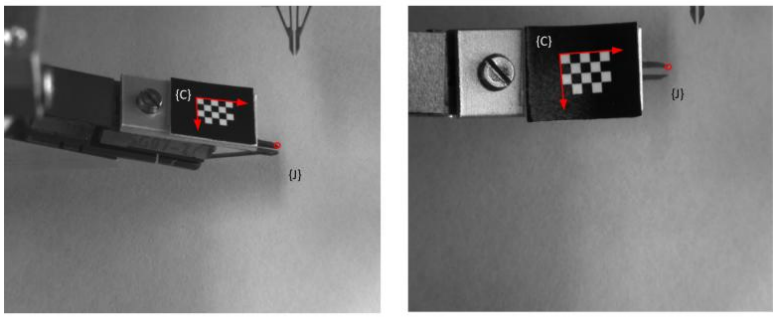

Fig. 4 Spatial relationship between the chessboard and gripper jaw from top and side views

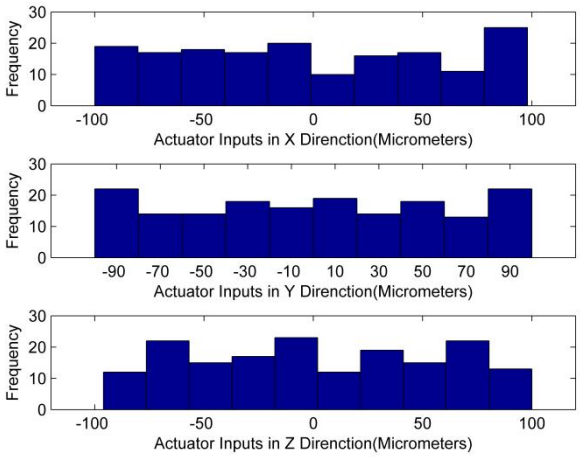

Fig. 5 Distribution of the actuator input commands for the calibration

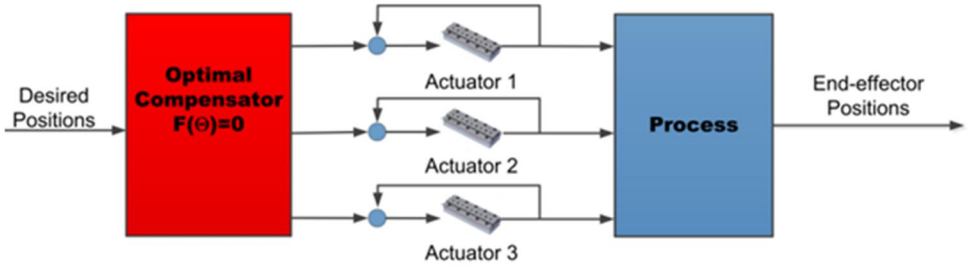

Fig. 6 The optimal compensator-based feedforward control

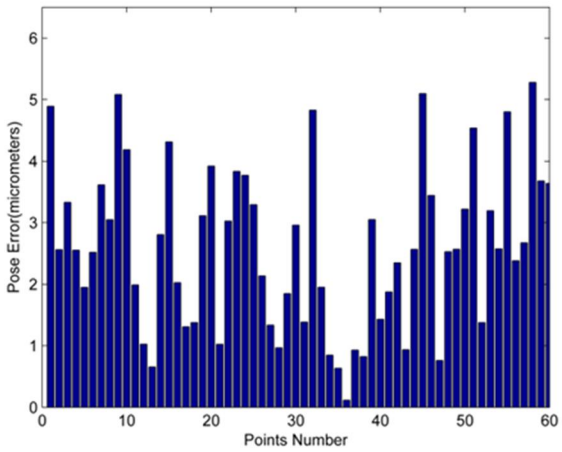

Fig. 7 The prediction errors of 60 validation points

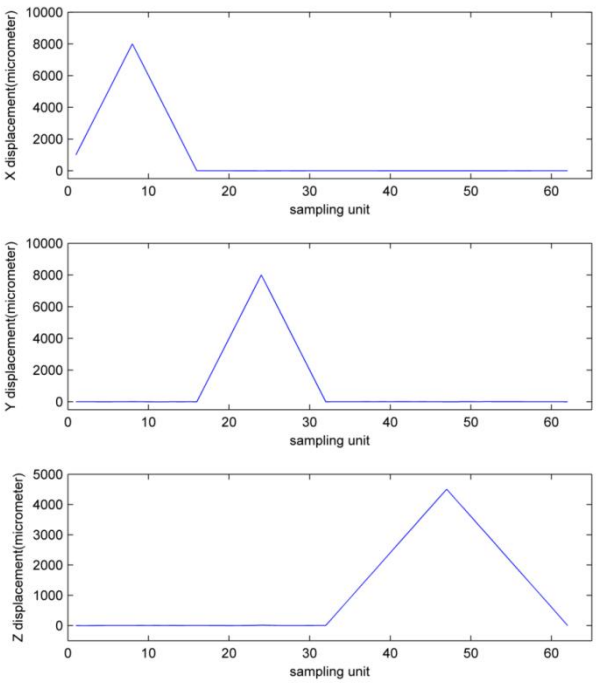

Fig. 8 Reference signal for the micromanipulator

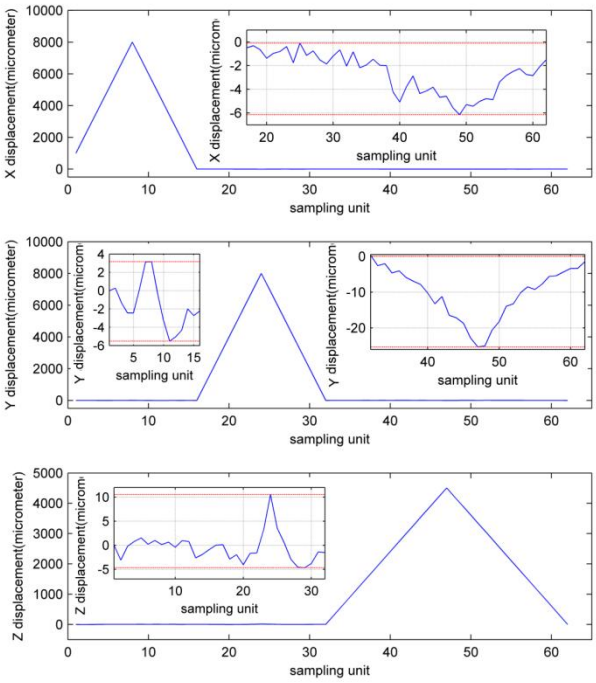

Fig. 9 Displacements of the micromanipulator for the decoupled motions (without calibration)

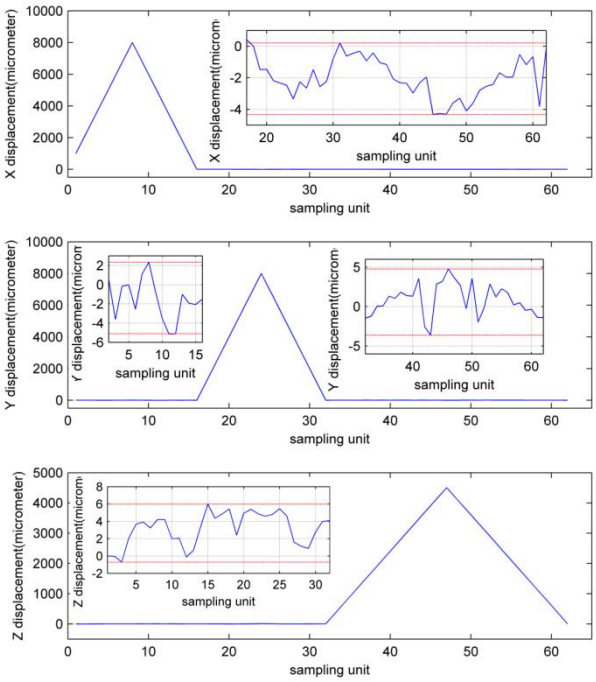

Fig. 10 Displacements of the micromanipulator for the decoupled motions (with optimal compensator)

Table 1 Selected list of publications in the field of microrobotic calibration

Years	Authors	Measurement Methods	DOF Motions	Depth(Z axis) Measurement Methods
1993 [20]	Arai, et al.	Microscope + Camera	X-Y-Z	Scale Measuring
1999 [13]	Kawaji, et al.	Microscope + Camera	X-Y-Z	Micro-Scale Measuring
2002 [14]	Li and Xi	Microscope + Camera	α-β-γ	-----
2006 [19]	Zhou, et al.	Laser	X-Y-Z	Laser Measuring
2009 [16]	Zhang, et al.	Microscope + Camera	X-Y-Z	Autofocusing
2009 [17]	Mattos and Cladwell	Microscope + Camera	X-Y-Θ	-----
2010 [15]	Liu, et al.	Microscope + Camera	X-Y-Θ	-----
2012 [18]	Tan, et al.	Microscope + Camera	X-Y-Θ	——

Table 2 Comparison between One Point Method and Virtual Points Method

Measurement Method	**Standard Deviation of Measurement**	
	x direction (Pixels)	***y direction(Pixels)***
One Point Method	0.207	0.172
Virtual Point Method	0.087	0.045